Internal Report
DESY M 06-02
July 2006

Computations of Wakefields for Beam Position Monitors of PETRA III

A.K. Bandyopadhyay, A. Jöstingmeier, A.S. Omar, R. Wanzenberg

Deutsches Elektronen-Synchrotron DESY, Hamburg

Internal Report
DESY M 06-02
July 2006

Computations of Wakefields for Beam Position Monitors of PETRA III

A.K. Bandyopadhyay[1], A. Jöstingmeier[1], A.S. Omar[1], and R. Wanzenberg[2]

[1]Chair of Microwave and Communication Engineering , Otto-Von-Guericke University, Magdeburg, Germany.
[2]Deutsches Elektronen Synchrotron, DESY, Notkestr. 85, Hamburg, Germany.

July 13, 2006

Abstract

At DESY it is planned to convert the existing PETRA II accelerator into a 3rd generation synchrotron radiation source, called PETRA III. The reconstruction will start mid 2007. The vacuum system of the 2.3 km long ring will be renewed. For proper design of PETRA III it is important to estimate the wakes due to various components along the beam pipe. This article covers the wake computations for two types of Beam Position Monitors (BPMs) for PETRA III. The computer codes MAFIA and Microwave Studio were used to compute the electromagnetic field. Convergence tests and the agreement between the results of both codes were taken as criteria in order to validate the results.

1 Introduction

In order to meet the future demands for synchrotron radiation at DESY it has been decided to convert the existing storage ring PETRA II into a 3rd generation synchrotron radiation source, called PETRA III [1]. The new light source will be operated at an energy of 6 GeV, a horizontal beam emittance of 1 nm and a vertical beam emittance of 0.01 nm. It is foreseen to install thirteen insertion devices in one octant ring, since this is an effective solution in terms of cost and constructional changes. The optic of the *new octant* consists of nine double bend achromat (DBA) cells, while 14 FODO cells are used in each of the seven other (often called old) octants. In the new octant a very good beam position monitor resolution of less then 1 μm in the vertical plane is require to stabilize the orbit with a feedback system to the level of 1 / 10 of the beam rms beam size. In the seven old octants a BPM resolution of about 10 μm is sufficient.

The standard vacuum chamber in the seven old octants has an elliptical shape with a total width of 80 mm and a total height of 40 mm. The elliptical vacuum chamber is often approximated with an octagonal shape for many numerical calculations with the computer

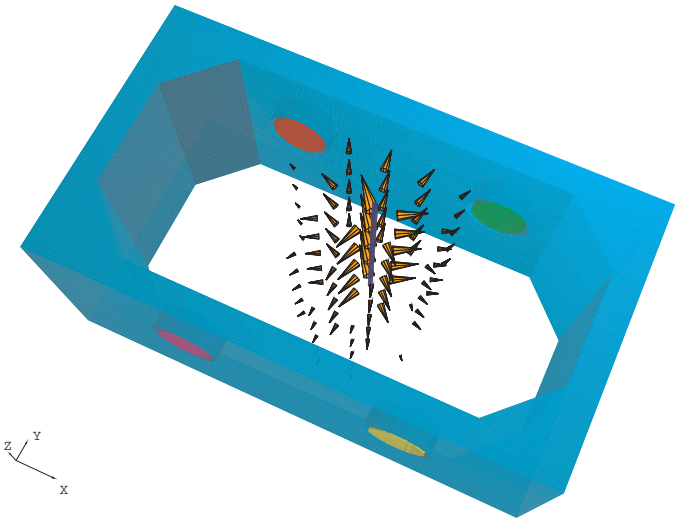

Figure 1: Electric (static) field of a line charge density in a beam position monitor.

code MAFIA. In Fig. 1 the electric field of a line charge density in a beam position monitor with four knobs as pick-up antennas is show. The corresponding electrostatic potential in the center of the BPM is show in Fig. 2. The beam position can be calculated from the four

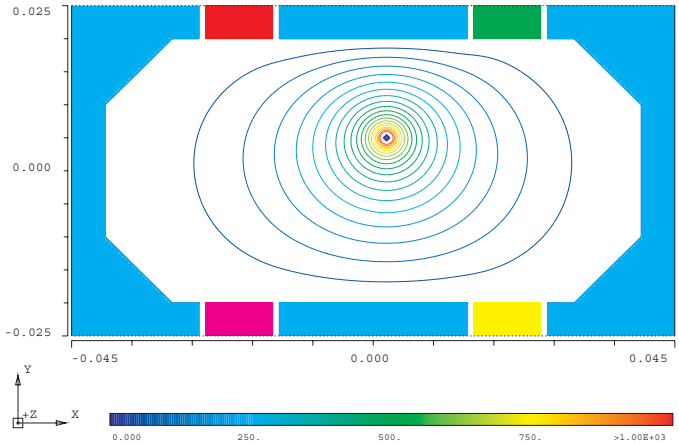

Figure 2: Electric (static) field of a line charge density in a beam position monitor.

pick-up signals Φ_{UR}, Φ_{UL}, Φ_{DR} and Φ_{DL} at the four button locations up-right (UR), up-left (UL), down-right (DR) and down-left (DL). The schematic allocation of signals at the buttons is shown in Fig. 3. The four button signals can be combined into a horizontal and a vertical normalized signal Φ_H and Φ_V according to the equations 1 and 2:

$$\Phi_H = \frac{(\Phi_{UR} + \Phi_{DR}) - (\Phi_{UL} + \Phi_{DL})}{\Phi_{UR} + \Phi_{UL} + \Phi_{DR} + \Phi_{DL}}, \tag{1}$$

$$\Phi_V = \frac{(\Phi_{UR} + \Phi_{UL}) - (\Phi_{DR} + \Phi_{DL})}{\Phi_{UR} + \Phi_{UL} + \Phi_{DR} + \Phi_{DL}}. \tag{2}$$

The vertical and horizontal signals Φ_H and Φ_V are functions of the beam positions (x_b, y_b). The vertical and horizontal monitor constants K_H and K_V are derived as the inverse of the

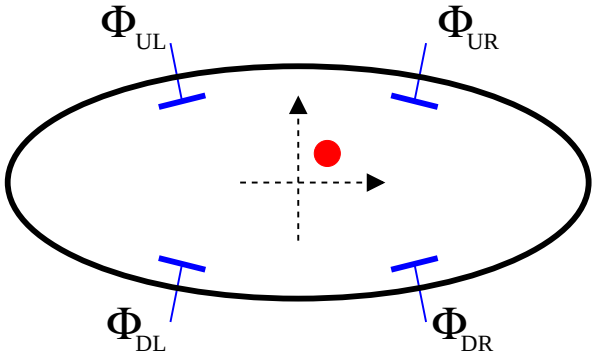

Figure 3: Allocation of pick-up signals of a BPM with four buttons.

derivative of the functions Φ_H and Φ_V evaluated at the origin:

$$\frac{1}{K_H} = \frac{\partial}{\partial x}\Phi_H \ (x=0, y=0), \qquad \frac{1}{K_V} = \frac{\partial}{\partial y}\Phi_V \ (x=0, y=0). \tag{3}$$

The beam positions can be calculated from the horizontal and vertical signal Φ_H and Φ_V in a linear approximation as:

$$x = K_H \ \Phi_H, \qquad y = K_V \ \Phi_V. \tag{4}$$

Several electrostatic calculations, similar to that shown in Fig.2, would be necessary to obtain the normalized potentials Φ_H and Φ_V as functions of position of the line charge (beam) position (x, y). A more practical way is the solution of a transformed electrostatic problem using Green's reciprocity theorem [2, p. 43] and the superposition principle. The transformed problem is an electrostatic problem with a fixed potential of one volt at one of the button electrodes and *no* line charge inside the vacuum chamber. The electrostatic potential is shown in Fig. 4. For the considered geometry one obtains the monitor constants

$$K_H = 14.2\,\mathrm{mm} \qquad K_V = 28.2\,\mathrm{mm}, \tag{5}$$

which implies that the monitor is less sensitive in the vertical plane than in the horizontal plane. A more balanced design ($K_H \approx K_V$) can be obtained if the positions of the pick-up electrodes in the vacuum chamber is optimized. Nevertheless the design shown in Fig. 2 has been used to calculate the wake fields due to the BPMs.

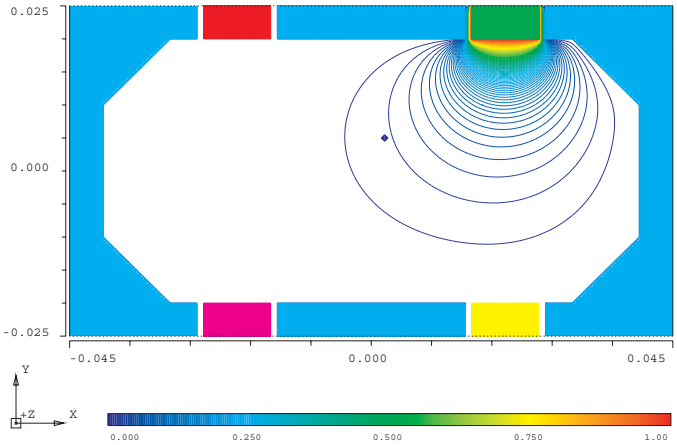

Figure 4: Electric (static) field of a line charge density in a beam position monitor.

2 Wakes

A beam in a storage ring interacts with its surroundings via electromagnetic fields induced by image currents in the walls of the vacuum chamber and in any other objects like RF cavities, kickers or beam positions monitors, which are considered in the next section of this report. These electromagnetic fields act back on the beam and may cause beam instabilities.

Two different bunch fill patterns with a total beam current of 100 mA are foreseen for PETRA III, one with many (960) bunches and a low single bunch intensity, and another one with only 40 bunches and a single bunch intensity of $24 \cdot 10^{10}$ electrons or positrons per bunch (2.5 mA single bunch current). In order to avoid intensity limitations, it is required to know the interaction of the beam with its surrounding. This interaction is described in detail by the wakefields excited due to a moving bunch of particles. From the wakefields several quantities, including the loss and kick parameters, are calculated which represent an integral measure of the interaction with the considered component of the accelerator.

Let us consider a point charge moving in free space at a velocity close to the velocity of light, c. With reference to the laboratory frame, the electric and magnetic fields of such a relativistic particle lie nearly in a plane passing through the charge and perpendicular to its path. So, a second charge moving behind the first charge on the same or on a parallel path, and at the same velocity $v \approx c$ will not be subjected to any forces from the fields produced by the leading charge. The situation is different if the two charges are moving in the vicinity of metallic objects or other boundary discontinuities. The trailing charge still will not experience the direct fields in the wavefront moving with the lead charge. This wavefront can, however, scatter from the boundary discontinuities, and this scattered radiation will be able to reach the trailing charge and exert forces parallel and perpendicular to its direction of motion. These scattered waves are termed wakefields, and the integrated effects of these wakefields over a given path length of the trailing charge give rise to longitudinal and transverse wake potentials [3–5].

Consider the situation shown in Fig. 5. A test charge q_2 follows a point charge q_1 at a

distant s. The Lorentz force on the test charge due to the fields generated by the point charge q_1 is

$$\vec{F} = \frac{d\vec{p}}{dt} = \; q_2\,(\vec{E} + c\,\vec{e_z} \times \vec{B}). \tag{6}$$

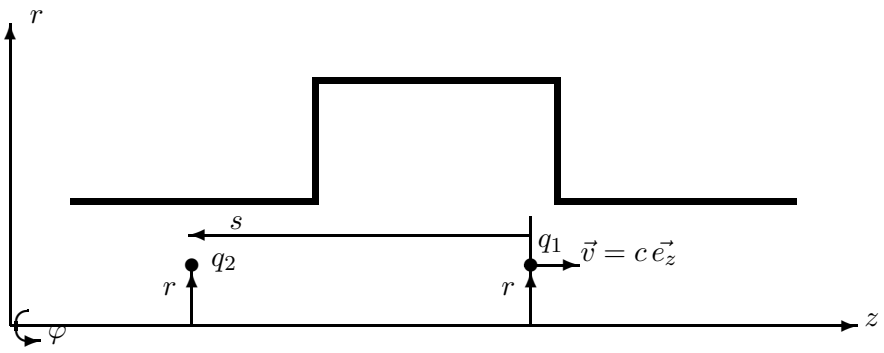

Figure 5: A point charge q_1 traversing a cavity with an offset r followed by a test charge q_2 with the same offset.

The **wake potential** of the point charge q_1 is defined as:

$$\vec{W}^{\delta}(r,s) = \frac{1}{q_1} \int_0^L dz\,(\vec{E} + c\,\vec{e_z} \times \vec{B})_{t=(z+s)/c}. \tag{7}$$

The wake potential may be regarded as an average of the Lorentz force on a test charge. Causality requires $\vec{W}(s) = 0$ for $s < 0$. The distant s is positive in the direction opposite to the motion of the point charge q_1. The wake potential of a Gaussian bunch with charge density:

$$\rho(\vec{r},t) = q_1\;\lambda(z-ct), \qquad \lambda(s) = \frac{1}{\sigma\sqrt{2\pi}} \exp\left(-\frac{(s-s_0)^2}{2\,\sigma^2}\right)$$

is obtained by a convolution integral with the point charge wake potential $\vec{W}^{\delta}$

$$\vec{W}(r,s) = \int_0^{\infty} ds'\,\lambda(s-s')\,\vec{W}^{\delta}(r,s').$$

From the wake potential $\vec{W}(s)$ of a Gaussian bunch the following loss and kick parameters are obtained:

$$k_{\parallel} \;=\; \int_{-\infty}^{\infty} ds\,W_{\parallel}(r=0,s)\,\lambda(s) \tag{8}$$

$$k_{\parallel}(1) \;=\; \int_{-\infty}^{\infty} ds\,W_{\parallel}(r=0,s)\,\frac{d}{ds}\lambda(s) \tag{9}$$

$$k_{\perp} \;=\; \frac{1}{r}\int_{-\infty}^{\infty} ds\,W_{\perp}(r,s)\,\lambda(s). \tag{10}$$

In the case that the total charge of the Gaussian bunch is q_1, the total energy loss of the bunch [6, 7] is given by,

$$\Delta W = q_1^2 \, k_{\parallel}. \tag{11}$$

The parameter $k_{\parallel}(1)$ plays an important role for the longitudinal impedance model of the accelerator [8]. From the parameter $k_{\parallel}(1)$ and the kick parameter $k_{\perp}$ the coherent tune shifts of the lowest order bunch modes in the longitudinal ($\Delta\nu_s$) and transverse planes ($\Delta\nu_\beta$) can be calculated according to the following equations [1, 8]:

$$\Delta\nu_s = \nu_s \frac{I_B \, R \, T_0}{2 \, h \, U_{\rm rf}} k_{\parallel}(1) \tag{12}$$

$$\Delta\nu_\beta = \frac{I_B \; < \beta > \; T_0}{4\pi \, E/e} k_{\perp}, \tag{13}$$

where $\nu_s = 0.045$ is the synchrotron tune, I_B the single bunch current, $R = 366.7$ m the average radius, $T_0 = 7.685\,\mu$s the revolution time, $h = 3840$ the harmonic number, $U_{\rm rf} = 20$ MV the total rf voltage, $< \beta >$ the average beta-function and $E = 6$ GeV the energy of PETRA III.

3 Simulation Software

3.1 Microwave Studio

CST MICROWAVE STUDIO ($MWST$) [9] is an electromagnetic field simulation code for the analysis and design of components such as antennas, filters, transmission lines, couplers, resonators etc., which is based on the Finite Integration Technique (FIT) [10, 11]. The code contains four different solvers: a transient solver, a frequency domain solver, an eigenmode solver and a modal analysis solver. $MWST$ has a user-friendly, Windows-based interface to model three-dimensional (3D) structures. The code includes the option of user defined or automatic meshing and features a Perfect Boundary Approximation (PBA) method. This method allows mesh cells to be partially filled for a more accurate representation of shapes that do not conform to the Cartesian (x,y,z) or cylindrical (r, θ,z) coordinate systems.

3.2 MAFIA

$MAFIA$ is a general code for the computation of electromagnetic fields [12]. It is also based on the Finite Integration Technique (FIT). The program is modular and is divided into pre-processor, postprocessor and several time and frequency domain solvers as well special solvers for electro- and magnetic-static problems. It is possible to simulate a particle beam to exciting electromagnetic fields in a general (three dimensional) geometrical structure and to compute the resulting wake potentials, which makes the program suitable to be used for electromagnetic problems related to particle accelerators.

4 The BPMs in the arc of PETRA III

For this article an elliptical beam pipe with the beam position monitor buttons positioned at an angle of $45°$ to the vertical axis is considered. This design is not optimal for the measurement of the beam position in the vertical plane (see also the discussion on monitor constants in the Introduction) and a modified design will be installed in PETRA III. The semi major axis and the semi minor axis of the normal beam pipe are 40 mm and 20 mm respectively. The cross section of the elliptical beam pipe along with the BPMs is shown in Fig. 6(a). Due to limitations for the shape creation and computer memory the elliptical structure was modeled in $MAFIA$ as an octagon. One quarter of the beam pipe as it was modeled in $MAFIA$ is shown in Fig. 6(b).

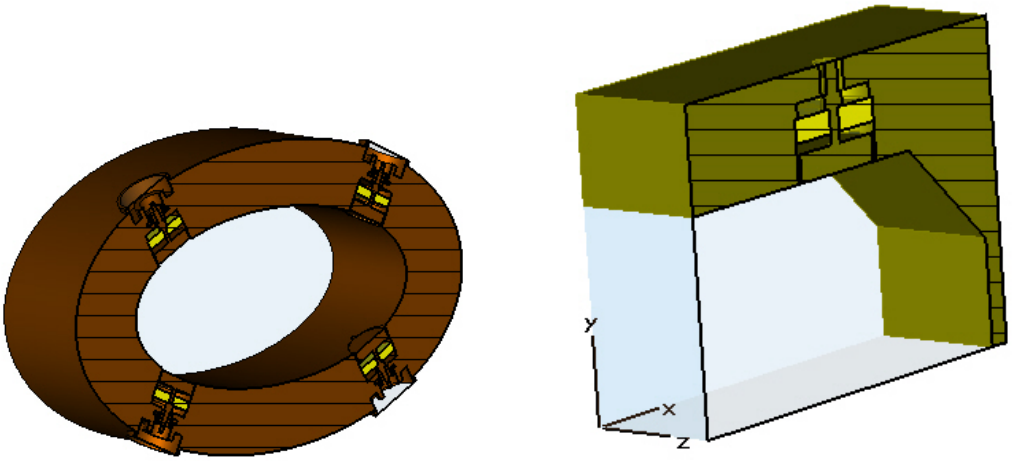

(a) The elliptical beam pipe with the BPMs.

(b) Quarter of the modeled beam pipe using $MAFIA$

Figure 6: The elliptical beam pipe and the same beam pipe as modeled for the $MAFIA$ simulations.

The auto-mesh facility within $MWST$ was used to model the beam pipe with the BPM, while the $MAFIA$ mesh was created manually. A comparison of the $MAFIA$ and $MWST$ meshes is shown in Fig. 7 and Fig. 8. It can be noticed that $MWST$ allows partially filled meshes, whereas $MAFIA$ supports only diagonal meshes. So the $MWST$ model is more realistic than the $MAFIA$ model. This difference is prominent for the BPM, as they consist of many small cylindrical shapes.

4.1 Eigenmode solver results

The eigenmode solver of $MAFIA$ and $MWST$ were used to compute the eigenmodes for a 25 mm long section of the beam pipe with the BPM mounted in the structure. The eigenmode solver results from $MWST$ and $MAFIA$ corresponding to the boundary conditions tabulated in Table 1 are summarized in the Tables 2 and 3, respectively.

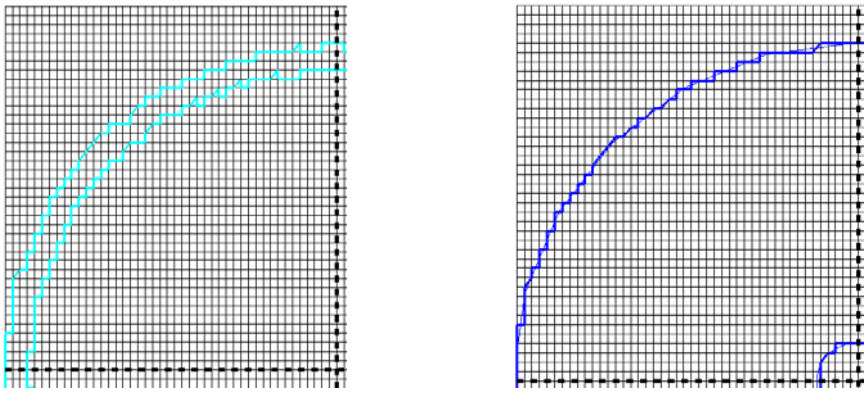

Figure 7: $MAFIA$ mesh of some parts of the BPM

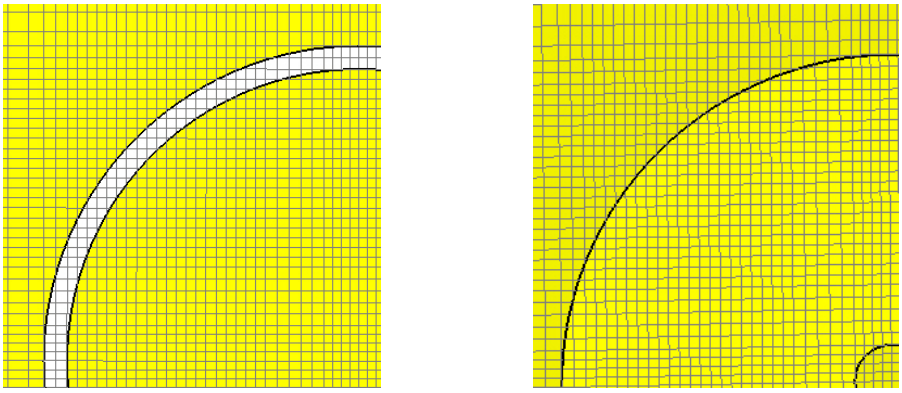

Figure 8: $MWST$ mesh of the same parts shown in Fig. 7

boundary	Boundary condition
x-min, x-max	Magnetic, Electric
y-min, y-max	Magnetic, Electric
z-min, z-max	Electric, Electric

Table 1: Boundary conditions used in $MWST$ and $MAFIA$ for the eigenmode computations with respect to the coordinate axes shown in Fig. 6

Solver Results:

Mode	Frequency	Accuracy |(Ax-x)/x|	max(e)	div(e)	rotrot(e)
1	1.92714241857	2.44e-010	2.21e-001	1.40e-007	2.88e-003
2	4.20936880627	6.35e-011	2.10e-002	3.23e-007	2.65e-004
3	6.87851293067	2.65e-012	8.67e-003	3.21e-007	1.01e-004
4	7.32856306526	9.68e-013	1.60e-002	3.01e-007	1.22e-004
5	7.50584843853	1.26e-012	9.82e-003	3.58e-007	1.12e-004
6	9.03549203027	1.13e-012	7.20e-003	2.11e-007	1.34e-004
7	9.03809142544	1.04e-012	7.13e-003	2.38e-007	1.27e-004
8	9.13007540136	5.89e-013	7.35e-003	2.94e-007	6.92e-005
9	9.59674813336	1.47e-012	1.48e-002	3.05e-007	8.59e-005
10	10.2229411257	4.34e-010	3.26e-003	2.29e-007	8.50e-005

Table 2: First ten eigenmodes computed using $MWST$ with the boundary conditions listed in Table 1.

summary of all modes found		maxwell's laws				solver accuracy
mode	frequency/hz	=div(d)= max norm	=div(b)= max norm	=curlcurl(e)= max norm	l2 norm	/Ax-lx/ /Ax/
1	1.862382E+09	1.3E-15	3.2E-14	1.7E-10	2.9E-12	8.0E-11
2	4.218702E+09	2.0E-14	1.5E-15	1.1E-10	5.1E-12	3.0E-11
3	6.887254E+09	4.0E-14	1.3E-15	1.3E-10	6.7E-12	4.5E-11
4	7.340331E+09	1.8E-14	2.9E-16	2.4E-11	2.5E-12	1.7E-11
5	7.506504E+09	4.6E-14	5.6E-16	2.6E-11	1.7E-12	4.3E-11
6	8.669406E+09	2.1E-14	3.7E-15	3.5E-11	3.6E-12	3.3E-10
7	8.692546E+09	3.3E-14	4.0E-15	4.5E-11	4.2E-12	2.8E-10
8	9.140355E+09	6.7E-13	5.2E-16	3.0E-09	2.0E-10	1.2E-09
9	9.583374E+09	2.0E-13	2.1E-16	1.4E-09	1.3E-10	2.1E-09
10	1.022856E+10	3.0E-13	1.9E-15	4.7E-09	6.0E-10	3.4E-08

Table 3: First ten eigenmodes computed using $MAFIA$ with the boundary conditions listed in Table 1

The eigenmode solver results from $MAFIA$ and $MWST$ corresponding to the boundary conditions shown in Table 4 are shown in the Tables 5 and 6, respectively. From the eigenmode solver results it may be noted that the eigenfrequencies for the **1st, 6th and 7th** eigenmodes do not change with the alternation of the boundary condition in the z-direction. The reason for this is that these three modes are concentrated near the BPM-button and therefore do not interact with the boundaries at z-min and z-max. The electric field plots for these modes are shown in the Figs. 9, 10, 11. The field plots clearly show that the energy of these modes is closely bound to the BPM itself. Here it may be noted that the $MWST$ results have

been used for the field plot as the modeling is more realistic with $MWST$.

boundary	Boundary condition
x-min, x-max	Magnetic, Electric
y-min, y-max	Magnetic, Electric
z-min, z-max	Magnetic, Magnetic

Table 4: Boundary conditions used in $MWST$ and $MAFIA$ for the eigenmode computations with respect to the coordinate axes shown in Fig. 6

Solver Results:

Mode		Frequency	Accuracy |(Ax-x)/x|	max(e)	div(e)	rotrot(e)
1		1.92827085477	3.29e-010	2.25e-001	1.45e-007	2.93e-003
2		4.5785644895	5.12e-011	2.60e-002	3.70e-007	2.68e-004
3		7.28619847313	2.32e-010	1.41e-002	4.12e-007	1.17e-004
4		7.44048054811	1.09e-010	2.60e-002	2.91e-007	1.21e-004
5		7.55333256074	1.36e-010	3.77e-003	3.50e-007	7.94e-005
6		8.91271191388	3.23e-008	7.19e-003	3.84e-007	1.22e-004
7	*	8.94042553942	5.26e-001	6.99e+001	2.43e-001	4.57e-001
8		9.02469094086	2.27e-008	7.17e-003	2.29e-007	1.33e-004
9		9.24912314321	9.22e-009	7.20e-003	4.12e-007	1.04e-004
10		9.61591057526	6.76e-012	9.24e-003	3.16e-007	7.78e-005

* = This mode has a bad accuracy.

Table 5: First ten eigenmodes computed using $MWST$ with the boundary conditions listed in Table 4.

summary of all modes found		maxwell's laws				solver accuracy
mode	frequency/hz	=div(d)= max norm	=div(b)= max norm	=curlcurl(e)= max norm	l2 norm	/Ax-lx/ /Ax/
1	1.887509E+09	7.5E-15	2.1E-14	1.3E-10	3.8E-12	2.2E-10
2	4.576678E+09	1.3E-14	2.8E-16	2.2E-11	1.8E-12	1.1E-11
3	7.277170E+09	3.1E-13	2.3E-15	2.8E-10	3.4E-11	5.1E-10
4	7.432736E+09	1.5E-13	2.9E-16	1.4E-10	1.7E-11	1.4E-10
5	7.549143E+09	1.8E-13	2.5E-16	2.0E-10	2.0E-11	1.3E-10
6	8.670643E+09	9.8E-13	4.1E-15	9.2E-10	1.3E-10	1.1E-08
7	8.701316E+09	4.4E-12	3.7E-15	4.4E-09	6.5E-10	5.5E-08
8	9.188983E+09	2.3E-12	2.7E-15	2.1E-09	3.3E-10	8.3E-09
9	9.587748E+09	2.8E-11	3.3E-16	4.5E-08	7.3E-09	1.6E-07
10	1.023401E+10	1.1E-07	1.1E-15	6.6E-04	1.1E-04	6.3E-03

Table 6: First ten eigenmodes computed using $MAFIA$ with the boundary conditions listed in Table 4.

The electric field plots corresponding to the modes 1, 6 and 7 computed with $MAFIA$ are shown in Figs. 12, 13 and 14, respectively. The two-dimensional plots of the electric field distribution in the vicinity of the BPM-button are also shown in 12, 13 and 14. The field distributions for the 6th and 7th modes indicate that these two modes are nearly degenerate orthogonally polarized dipole modes trapped in the vicinity of the BPM button.

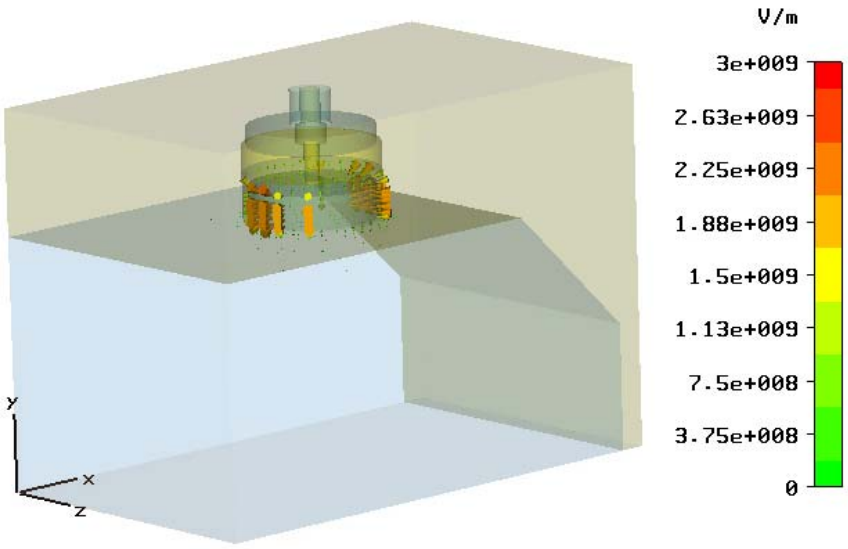

Figure 9: The electric field distribution corresponding to the first mode as calculated with $MWST$.

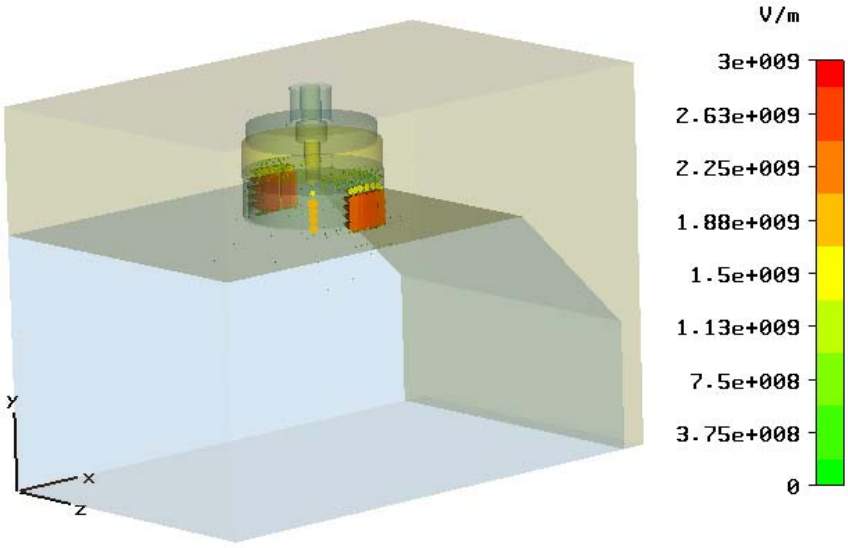

Figure 10: The electric field distribution corresponding to the sixth mode as calculated with $MWST$.

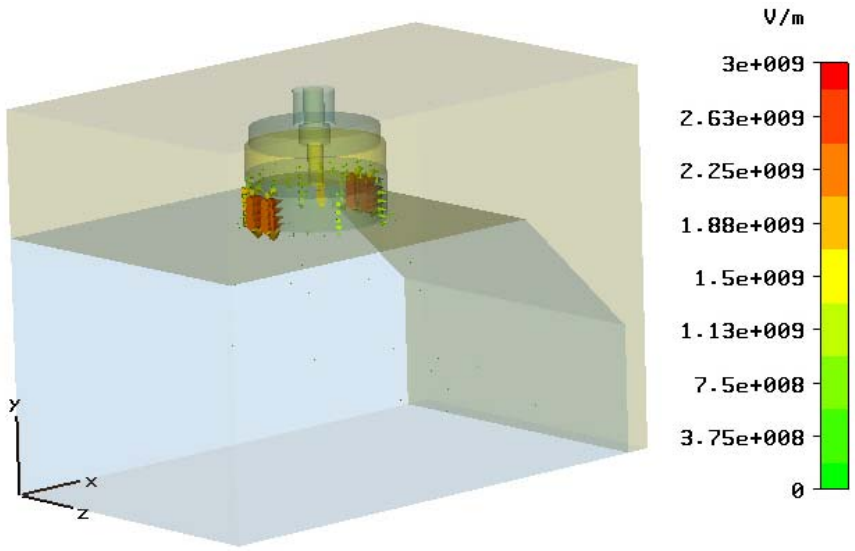

Figure 11: The electric field distribution corresponding to the seventh mode as calculated with $MWST$.

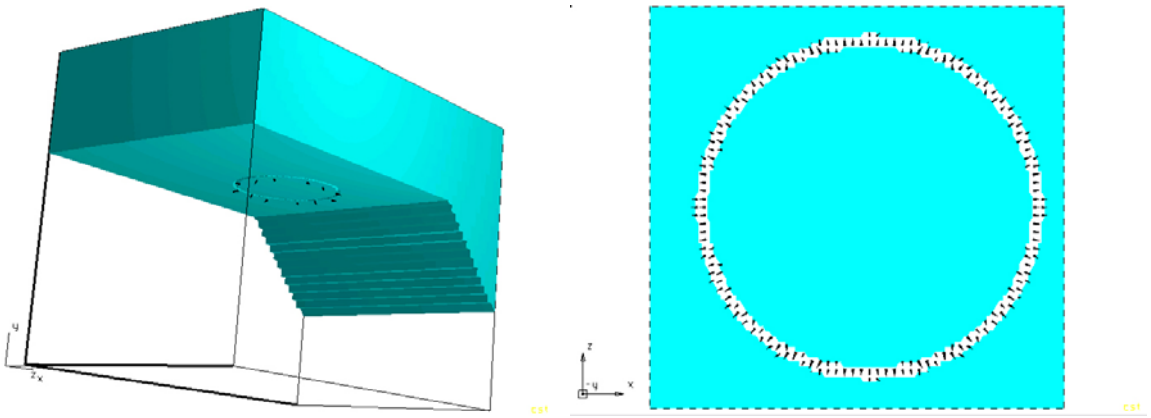

(a) Electric field distribution at the beam pipe for mode 1 from the $MAFIA$ eigenmode solver.

(b) Details of the electric field distribution near the button monitor of the BPM for mode 1 from the $MAFIA$ eigenmode solver.

Figure 12: Electric field distribution for mode 1 from the $MAFIA$ eigenmode solver.

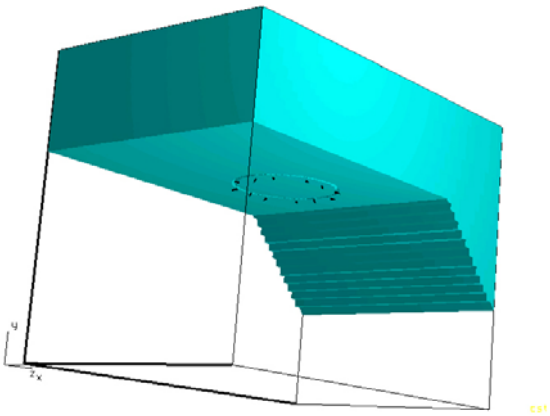

(a) Electric field distribution at the beam pipe for mode 6 from the $MAFIA$ eigenmode solver.

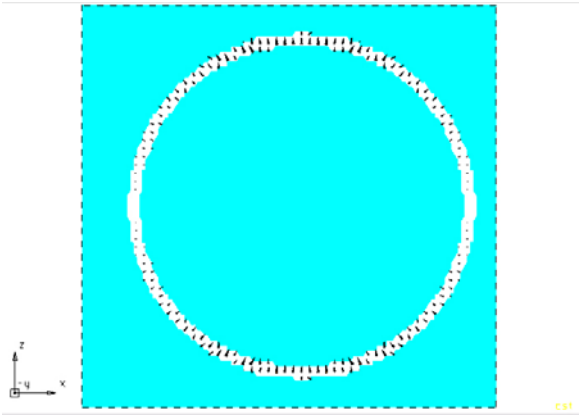

(b) Details of the electric field distribution near the button monitor of the BPM for mode 6 from the $MAFIA$ eigenmode solver.

Figure 13: Electric field distribution for mode 6 from the $MAFIA$ eigenmode solver.

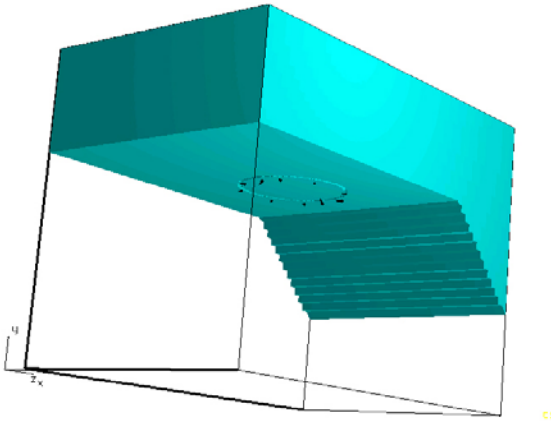

(a) Electric field distribution at the beam pipe for mode 7 from the $MAFIA$ eigenmode solver.

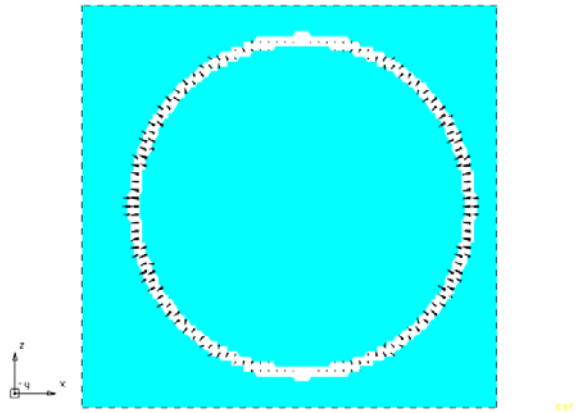

(b) Details of the electric field distribution near the button monitor of the BPM for mode 7 from the $MAFIA$ eigenmode solver.

Figure 14: Electric field distribution for mode 1 from the $MAFIA$ eigenmode solver.

4.2 Wake computation results

For the wake computations, the coaxial port of the BPM has been modeled as a waveguide port. To ensure that the port definition has been correctly implemented into the $MAFIA$ model, time domain simulations of scattering parameters for the same structure with $MAFIA$ and $MWST$ were compared. The boundaries in the z-direction were taken as electric boundaries. The phases of the reflection coefficient (S_{11}) recorded at the coaxial port computed with $MAFIA$ and $MWST$ are shown in Fig. 15. The good agreement between the obtained results strongly supports the accuracy of the computations. Here it may be mentioned that in reality the coaxial waveguide port should have a 50 Ω impedance. For the limitations in mesh resolution, the modeled waveguide port has an impedance of nearly 41 Ω.

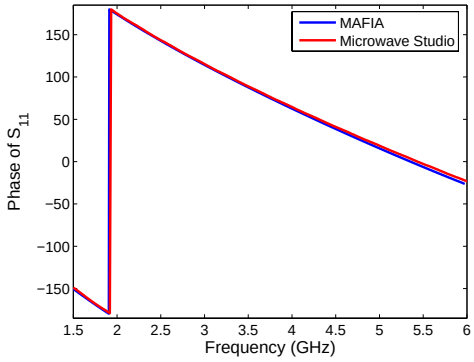

Figure 15: Comparison of frequency vs. phase of S_{11} computed with $MWST$ and $MAFIA$ at the coaxial BPM port.

In the next step, the time-domain computations for the wake fields were done. A beam with an rms bunch length (σ_z) of 10 mm, transversing the BPM on axis in the vacuum chamber, was used as the excitation source. For the simulation a Gaussian charge distribution with a total charge of 1 C was used. The beam pipe was considered to be 100 mm long, stretching equally at both sides of the discontinuity (the BPM). A cut through the geometry is shown in Fig. 16. A uniform mesh step size of 0.12 mm along the z-axis was used, which is a compromise between the available computer memory and the necessity to model the small gap of 0.4 mm between the BPM button and the vacuum chamber. The details of the meshing in the vicinity of the BPM can be seen in Fig. 17.

Here it may be mentioned that a new coordinate system is generally used to describe the positions of the particles in the bunch. This coordinate system is termed the 'bunch coordinate system'. This bunch coordinate system is specified by the two transverse Cartesian coordinates which are the same as before and a new coordinate axis 's' along the beam axis. The orientation of this s-axis is opposite to the direction in which the beam moves. The origin of the bunch coordinate system is moving with the bunch and is given by the position of the very first particle in the bunch. A wakefield monitor has been placed at $x = y = 0$ to record the wakefields as a function of the bunch coordinate (s). The z-component of the wake potential (longitudinal wake) and the bunch charge density versus the bunch coordinate are

shown in Fig. 18.

The total loss parameter computed according to equation (8) is found to be -4.0744×10^8 V/C. It sufficient to evaluate the integral in Eqn. (8) from zero to $10\,\sigma_z$ since the particle density is zero for $s > 10\,\sigma_z$. The trapezoidal rule was used for the integration and an interpolation of the wake data within the integration limit was used. The $k(1)$ parameter comes out to be $-1.0266 \times 10^{11}\,\mathrm{VC}^{-1}\,\mathrm{m}^{-1}$.

The wake calculations have been repeated with a finer mesh step. For a mesh size of 0.1 mm along the z-axis the loss parameter is -3.5276×10^8 V/C while the $k(1)$ parameter is $-9.0985 \times 10^{10}\,\mathrm{VC}^{-1}\,\mathrm{m}^{-1}$.

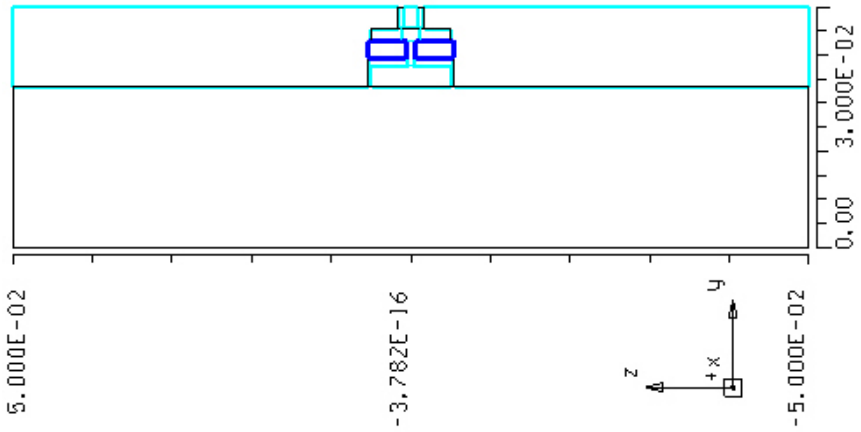

Figure 16: Cross section (YZ plane) of the beam pipe along with the BPM.

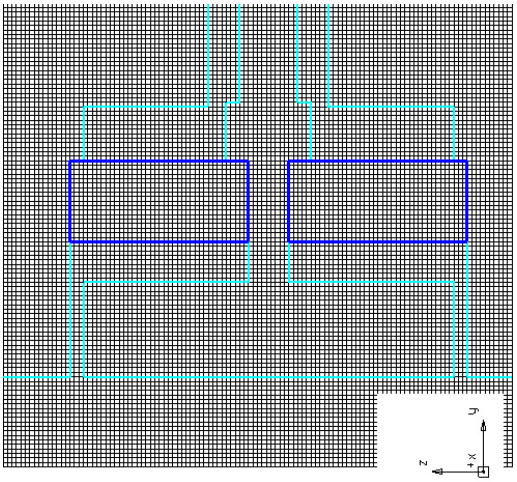

Figure 17: Detailed view of the mesh (YZ plane) for a part of the beam pipe containing the button monitor of the BPM.

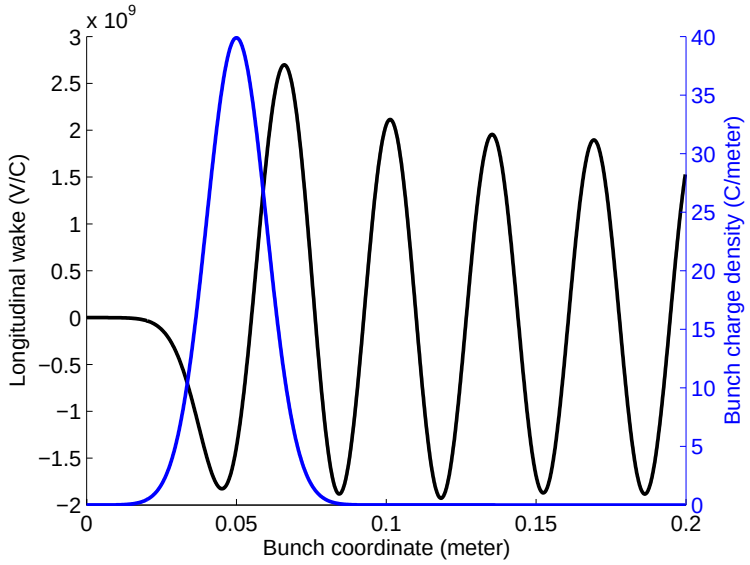

Figure 18: The z-component of the wake and the bunch charge density vs the bunch coordinate.

From the previous eigenmode computation, it has turned out that some of the eigenmodes are trapped in the vicinity of the BPM. These modes contribute significantly to the long range wake. To investigate this point in detail, electric field monitors (for all three components of the electric field) have been defined during the simulation time at a point near the BPM-button. The approximate position of the field monitor is shown by the arrow in Fig. 19.

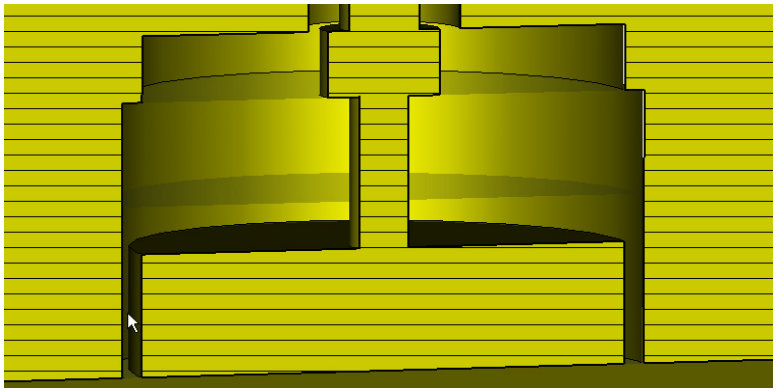

Figure 19: The position (indicated by the arrow) at which the electric field components are monitored.

The variation of the z-component of the electric field as a function of time at the monitor is plotted in Fig. 20. The frequency of the field is estimated from the time period. It comes out to be approximately 8.6 GHz - which is near to the frequencies of the 6^{th} and 7^{th} eigenmodes found with the eigenmode solver of $MAFIA$ and $MWST$.

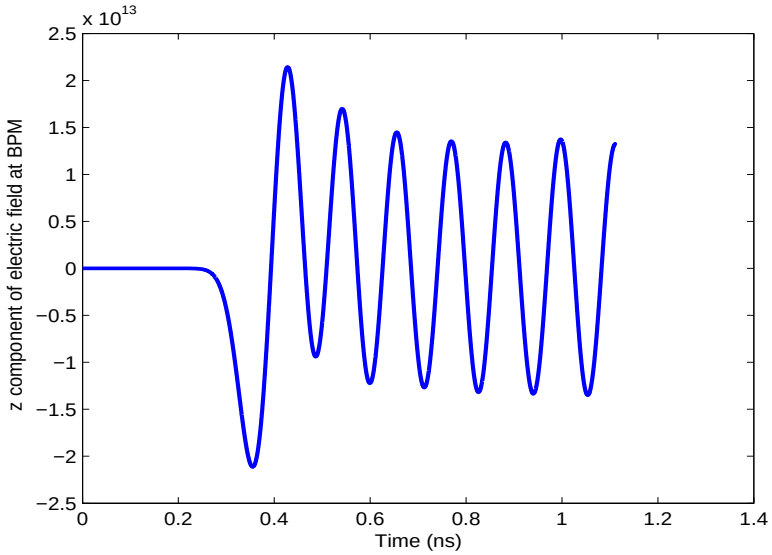

Figure 20: The z-component of the electric field vs time at the position indicated in Fig. 19.

4.3 Estimation of the quality factors and other cavity parameters

The quality factors of the modes 6 and 7 were calculated with the codes $MAFIA$ and $MWST$ using the power loss method. For these computations the conductivity of copper was taken as $5.8 \times 10^7 (\Omega \mathrm{m})^{-1}$. The dielectric constant and the loss tangent of the Al_2O_3 ceramic disk were taken as 9.5 and 5×10^{-4}, respectively. The quality factors obtained from $MWST$ are 758 and 847 for the 6^{th} and the 7^{th} mode, respectively. It has to be stated here that the frequencies of the 6^{th} and the 7^{th} modes from $MWST$ come out to be 9.036 GHz and 9.038 GHz, respectively. This is quite far apart from the corresponding resonant frequencies obtained using $MAFIA$ which are 8.712 GHz and 8.7476 GHz, respectively. The quality factors for the same modes obtained from $MAFIA$ are 753 and 707, respectively. The deviations of the resonant frequencies can be explained by the difference in modeling of the structure in $MAFIA$ and in $MWST$. In the $MAFIA$ calculations, the gap between the electrode of the button monitor and the shielding looks quite rough, whereas the accuracy of the $MWST$ model is much better due to the partially filled cells. However, the differences in the quality factors computed with $MAFIA$ and $MWST$ are in an acceptable range. Another point to keep in mind is that the actual surface resistance of the metallic parts of the structure is about 10% higher than the theoretical surface resistance - leading to a lower conductivity of copper than the theoretical one ($\sigma_{copper} = 5.8 \times 10^7 (\Omega\,\mathrm{m})^{-1}$) used for the loss calculations.

The loss parameter $k(\mathbf{r}_\perp)$, the shunt resistance $R(\mathbf{r}_\perp)$ and the parameter G_1 were calculated in the next step. First, the longitudinal voltage $V_L(\mathbf{r}_\perp)$ for the length of the beam pipe was obtained using the *#1dintegral* section of $MAFIA$ as,

$$V_L(\mathbf{r}_\perp) = \int_0^L E_z(\mathbf{r}_\perp, z)\, \exp(-i\omega z/c) dz \tag{14}$$

where $\mathbf{r}_\perp$ is the transverse offset and z is the coordinate in the axial direction of the beam pipe. The electric fields corresponding to modes 6 and 7 were used, and the integration path was taken from $(0.0, \textit{yoffset}, \textit{zmin})$ to $(0.0, \textit{yoffset}, \textit{zmax})$. The total energy of the mode is calculated (considering the symmetries) by default in $MAFIA$ as

$$U = \frac{\epsilon_0}{2} \int |\mathbf{E}|^2 d^3 r. \tag{15}$$

From the voltage and the total energy stored, the modal loss parameter $k(\mathbf{r}_\perp)$, the shunt resistance $R_{shunt}(\mathbf{r}_\perp)$ and the parameter G_1 were calculated according to the following equations:

$$k(\mathbf{r}_\perp) = \frac{|V_L(\mathbf{r_1})|^2}{4 \times U} \tag{16}$$

$$R_{shunt}(\mathbf{r_1}) = \frac{|V_L(\mathbf{r}_\perp)|^2}{2 \cdot P_w} \tag{17}$$

$$G_1 = R_{cu} \times Q, \tag{18}$$

where R_{cu} is the surface resistivity of copper and P_w is the metallic power losses. The values of G_1 was found to be 18.3 Ω and 17.3 Ω for the 6^{th} and the 7^{th} mode, respectively. The plots of the loss parameter and the shunt resistance as a function of *yoffset* are shown in Figs. 21 and 22 respectively.

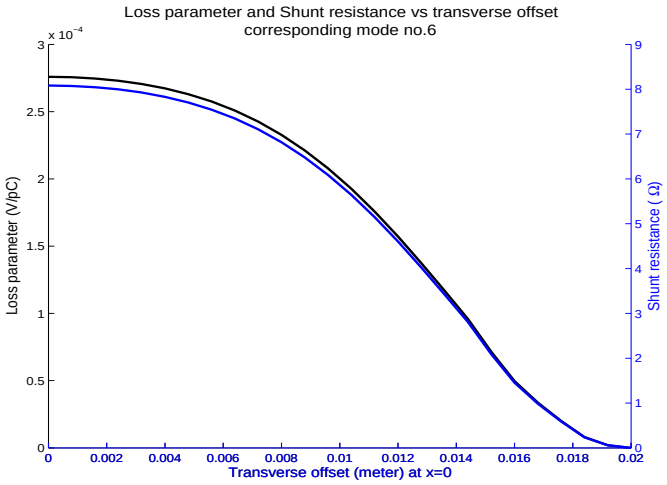

Figure 21: The loss parameter and the shunt resistance corresponding to mode 6 (frequency $= 8.6694$ GHz) as a function of the offset in the y-direction.

4.4 Wake computations for an off-axis beam

The next step was to compute the wakes for an off axis beam. In this case it is no longer sufficient to consider one quarter of the structure since the symmetry for at least plane is lost. Therefore one half (considering a beam offset in only one transverse direction) of the beam

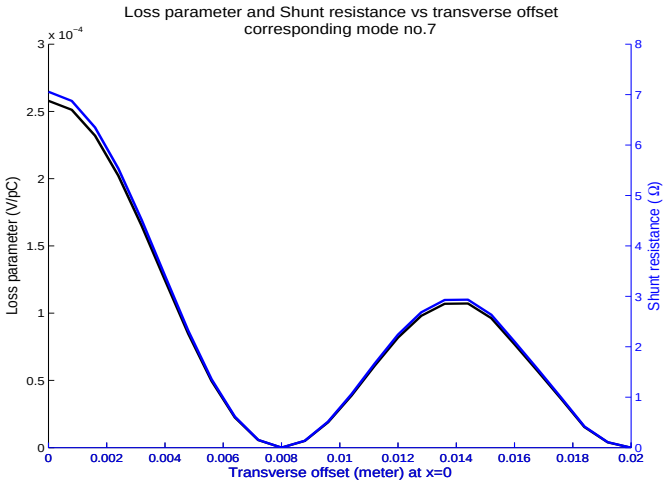

Figure 22: The loss parameter and the shunt resistance corresponding to mode 7 (frequency $= 8.6925\ GHz$) as a function of the offset in the y-direction.

pipe has been modeled instead of only one quarter. A cut along the z-axis and a cross section of the beam pipe as modeled in $MAFIA$ for wake computations for a beam with a y-offset are shown in Figs. 23 and 24, respectively.

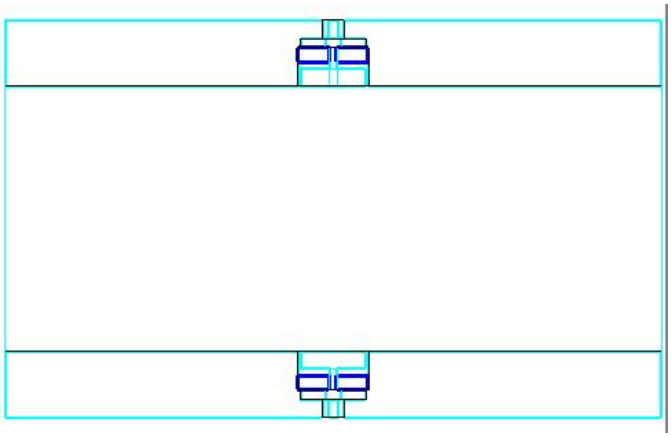

Figure 23: Longitudinal section of the beam pipe (normal to the x-direction) modeled with $MAFIA$ with the cutting plane located at the center of the BPMs.

For the wake computations, both the upper and the lower coaxial ports were modeled as waveguide ports. The simulation results for the longitudinal wake, y-component of the wake and the output wave amplitudes at both coaxial waveguide ports are shown in the Figs. 25, 26 and 27, respectively. In this case an offset of 5 mm in the y-direction was considered. The wave amplitude recorded at the upper and the lower coaxial ports are different, as is expected. The wave amplitude at the upper coaxial port is larger than that at the lower port

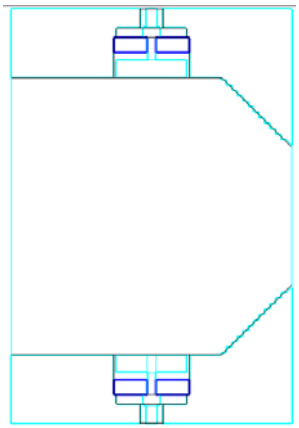

Figure 24: Cross section of the beam pipe (normal to the z-direction) modeled with $MAFIA$.

because the beam is now nearer to the upper coaxial port. The difference between these two wave amplitudes has also been plotted versus time in the same graph. The loss parameter ($k_{\|}$) and the $k_{\|}(1)$-parameter computed according to equations (8) and (9) for a 5 mm y-offset of the bunch are found to be -3.9167×10^8 V / C and -9.8876×10^{10} $\mathrm{VC}^{-1}\mathrm{m}^{-1}$, respectively. With a finer meshing, the same parameters come out to be -3.3527×10^8 V / C and -8.6656×10^{10} $VC^{-1}m^{-1}$, respectively.

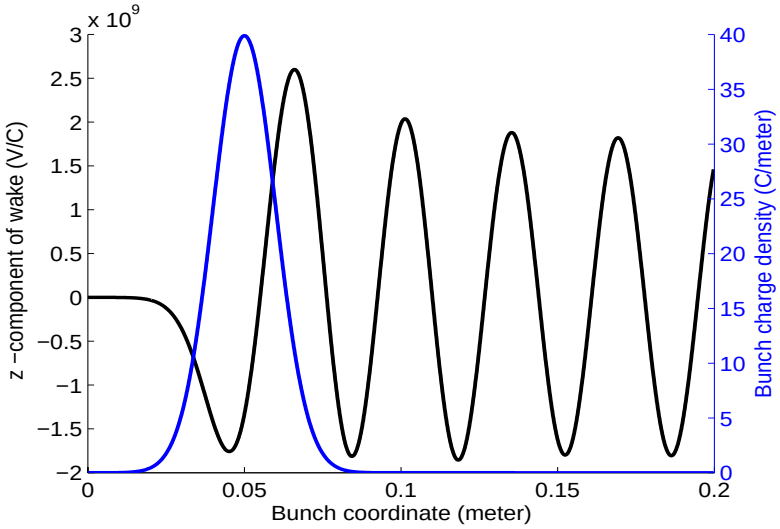

Figure 25: The z-component of the wake potential and the bunch charge density vs the bunch coordinate for a 5 mm y-offset of the beam (coarse mesh).

The kick parameter has been calculated using equation (10) and the y-component W_y of the wake potential. The y-kick parameter, normalized to the y-offset of 5 mm, comes out to be $-17.842 \times 10^9\,\mathrm{V}/(\mathrm{C\,m})$. The same parameter with a finer mesh comes out to be

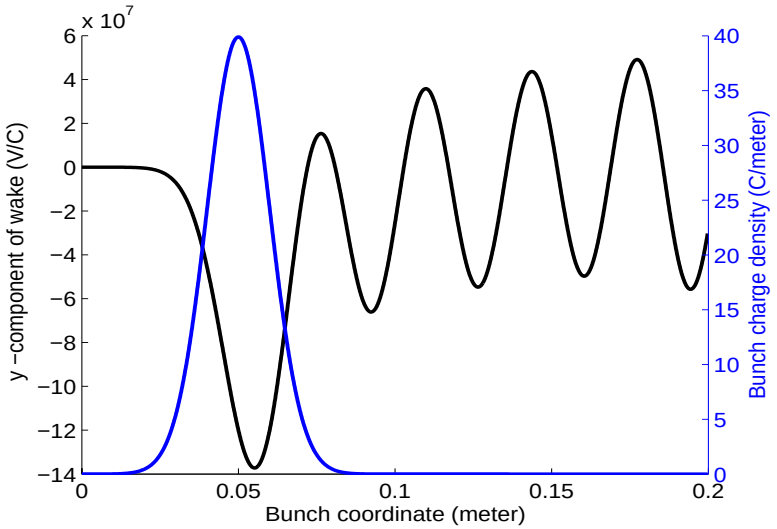

Figure 26: The y-component of the wake potential and the bunch charge density vs the bunch coordinate for a 5 mm y-offset of the beam (coarse mesh).

$-25.256 \times 10^9\,\mathrm{V/(C\,m)}$.

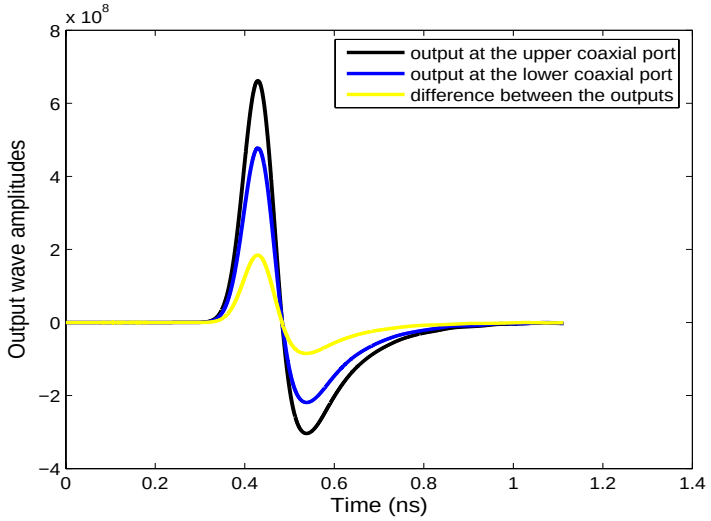

Figure 27: The output wave amplitude vs time at the coaxial ports for a y-offset of 5 mm (coarse mesh).

5 Modeling of the BPM near the undulator chamber

The design of the BPM close to the undulator chamber is not yet finalized. For a first evaluation of the wake fields due to this BPM we have modeled a button BPM in the undulator chamber with four buttons similar to the BPM in the arc. The cross-section of the beam pipe is, in this case, also an ellipse, but the minor axis is much smaller (minor axis = 7 mm, major axis = 90 mm) than that of the arc beam pipe. The BPM buttons are placed 5 mm apart from the center. The geometry and the dimensions of the BPM buttons and feed-throughs are taken to be the same as in the arc. To model the structure, as in the arc, the elliptical cross section of the beam pipe was approximated by a polygon. To be consistent, the same approximations were used for modeling the beam pipe with $MAFIA$ and with $MWST$. The $MWST$ model for the approximated structure is shown in Fig. 28. The corresponding meshing in the vicinity of the BPM is shown in Fig. 29. The eigenmode solver results obtained by $MWST$ corresponding to the boundary conditions listed in Table 7 are shown in Table 8.

boundary	boundary condition
x-min,x-max	Magnetic,Electric
y-min,y-max	Magnetic,Electric
z-min,z-max	Electric,Electric

Table 7: Boundary conditions used in $MWST$ and $MAFIA$ for the eigenmode computations.

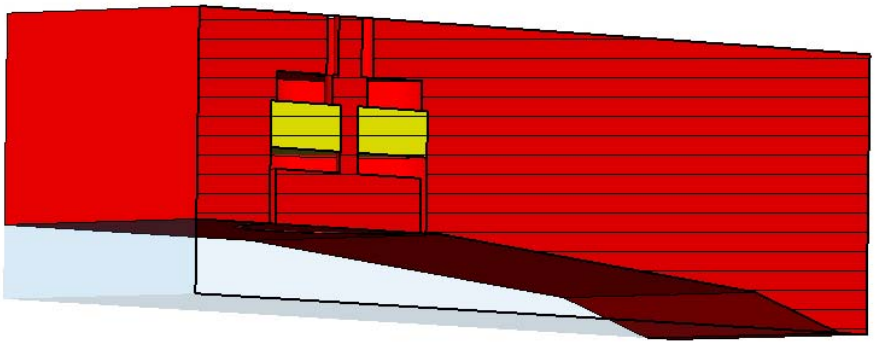

Figure 28: The BPM near the undulator chamber and a quarter of the beam pipe as modeled in $MWST$.

The list of the first ten eigenmodes computed using $MWST$ and $MAFIA$ corresponding to the boundary conditions tabulated in Table 9 are given in Tables 10 and 11 respectively. Comparison of the obtained results using both programs underlines the quality of the results. The resonant frequencies computed with both programs agree very well. Here, it may be noted that the frequencies of the eigenmodes are the same as those found with electric wall boundary conditions at z-min and z-max. As the resonant frequencies are not affected at all by the z boundaries, it can be concluded that all of the computed eigenmodes in Tables 10 and 11 are confined near the the BPM.

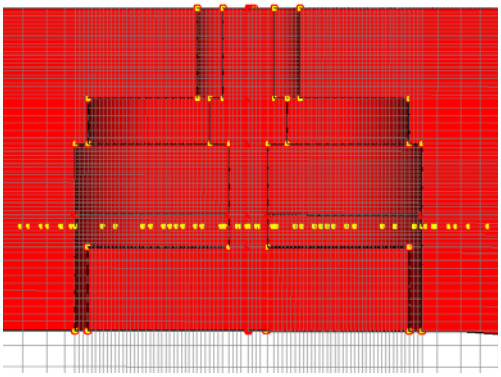

Figure 29: Mesh distribution in the vicinity of the BPM.

Solver Results:

Mode	Frequency	Accuracy			
		|(Ax-x)/x|	max(e)	div(e)	rotrot(e)
1	1.92726463108	5.78e-009	4.62e-001	1.73e-007	4.63e-003
2	8.99658585179	2.25e-010	1.51e-002	2.06e-007	2.11e-004
3	8.99840340114	2.00e-010	1.49e-002	2.06e-007	2.09e-004
4	10.217567149	7.63e-011	6.78e-003	2.70e-007	1.28e-004
5	13.6113432959	2.29e-010	6.30e-003	2.94e-007	7.17e-005
6	13.6126823839	4.27e-011	6.27e-003	2.95e-007	7.18e-005
7	14.508466979	3.14e-010	7.57e-003	3.17e-007	5.98e-005
8	14.5086275328	4.53e-010	5.16e-003	3.04e-007	5.71e-005
9	17.290027579	1.27e-008	2.11e-003	2.63e-007	1.83e-005
10	17.4849496707	3.56e-006	4.44e-003	2.98e-007	2.71e-005

Optimum guess for the highest eigenfrequency would be: 17.48

Table 8: Eigenmode solver results from $MWST$ corresponding to the boundary conditions of table 7.

boundary	Boundary condition
x-min, x-max	Magnetic, Electric
y-min, y-max	Magnetic, Electric
z-min, z-max	Magnetic, Magnetic

Table 9: Boundary conditions used in $MWST$ and $MAFIA$ for the eigenmode computations.

Solver Results:

Mode	Frequency	Accuracy			
		|(Ax-x)/x|	max(e)	div(e)	rotrot(e)
1	1.91620213801	5.33e-011	9.27e-002	9.14e-008	1.54e-003
2	8.97290248251	7.21e-013	3.48e-003	1.15e-007	7.87e-005
3	8.9739353717	1.10e-011	3.48e-003	1.14e-007	7.87e-005
4	10.167741881	2.92e-013	1.72e-003	1.49e-007	5.53e-005
5	13.5869433112	2.73e-013	1.47e-003	1.66e-007	2.71e-005
6	13.5878316673	1.54e-013	1.49e-003	1.65e-007	2.75e-005
7	14.503225816	2.63e-013	1.11e-003	1.80e-007	2.06e-005
8	14.5092572257	3.32e-013	1.22e-003	1.60e-007	2.16e-005
9	17.311131997	1.37e-010	5.69e-004	1.58e-007	6.46e-006
10	17.4844596848	6.12e-006	1.52e-003	2.93e-007	1.95e-005

Optimum guess for the highest eigenfrequency would be: 17.48

Table 10: First ten eigenmodes computed using $MWST$ with the boundary conditions listed in Table 9.

summary of all modes found		maxwell's laws				solver accuracy
mode	frequency/hz	=div(d)= max norm	=div(b)= max norm	=curlcurl(e)= max norm	=curlcurl(e)= l2 norm	/Ax-lx/ /Ax/
1	1.918552E+09	9.9E-16	2.8E-14	3.4E-10	5.6E-12	1.6E-10
2	8.791573E+09	4.7E-16	6.1E-15	1.6E-11	3.1E-13	2.0E-11
3	8.858154E+09	6.8E-16	5.3E-15	9.6E-12	1.2E-13	8.1E-12
4	1.025713E+10	4.5E-16	5.6E-15	2.1E-11	3.9E-13	2.7E-11
5	1.359069E+10	6.9E-16	2.3E-15	1.5E-11	2.9E-13	9.4E-12
6	1.360523E+10	8.6E-16	2.2E-15	3.5E-11	6.8E-13	1.8E-11
7	1.447176E+10	1.3E-15	2.0E-15	3.2E-11	6.1E-13	2.0E-11
8	1.449780E+10	1.5E-15	2.1E-15	1.2E-10	2.3E-12	6.5E-11
9	1.734803E+10	2.5E-14	2.6E-16	2.2E-07	4.3E-09	4.4E-08
10	1.750034E+10	1.4E-15	7.9E-16	2.3E-06	4.4E-08	6.8E-07

Table 11: First ten eigenmodes computed using $MAFIA$ with the boundary conditions listed in Table 9.

The electric field distributions for the first four modes are shown in Figs. 30, 31, 32 and 33. The field distribution plots were taken from $MWST$ simulations because of the convenience in displaying the results. The field plots confirm that all the eigenmodes are confined near the BPM.

The quality factors of all modes were computed both with $MAFIA$ and $MWST$. The quality factors for the first ten eigenmodes from $MWST$ and $MAFIA$ are listed in Table 12. For the quality factor computations, the conductivity of copper has been taken as $5.8 \times 10^7 (\Omega m)^{-1}$, the relative dielectric constant and the loss tangent of the alumina disk were taken as 9.5 and 5×10^{-4}, respectively. For a few modes, there is a good agreement between the computed quality factors using $MAFIA$ and $MWST$, but mostly for the modes with higher resonant frequencies, there is a quite large relative deviation between the computed quality factors. Apart from the difference between the loss modules implemented in $MWST$ and $MAFIA$, the deviation of the results may be explained by the different meshing schemes in both methods.

mode number	Frequency in GHz (MWST)	Frequency in GHz (MAFIA)	Q-value (MWST)	Q-value (MAFIA)	$\frac{Q_{MWST}-Q_{MAFIA}}{Q_{average}} \times 100\%$
1	1.9162	1.9186	774	933	-18.63
2	8.9729	8.7916	717	693	3.40
3	8.9739	8.8582	718	690	3.98
4	10.1677	10.2571	997	1037	-3.93
5	13.5869	13.5907	1602	1361	16.26
6	13.5878	13.6052	1604	1360	16.46
7	14.5032	14.4718	1481	1158	24.48
8	14.5093	14.4978	1497	1188	23.02
9	17.3111	17.3480	2427	1561	43.43
10	17.4845	17.5003	2006	1377	37.19

Table 12: Quality factors computed with $MWST$ and $MAFIA$ and their relative deviations for the first 10 eigenmodes.

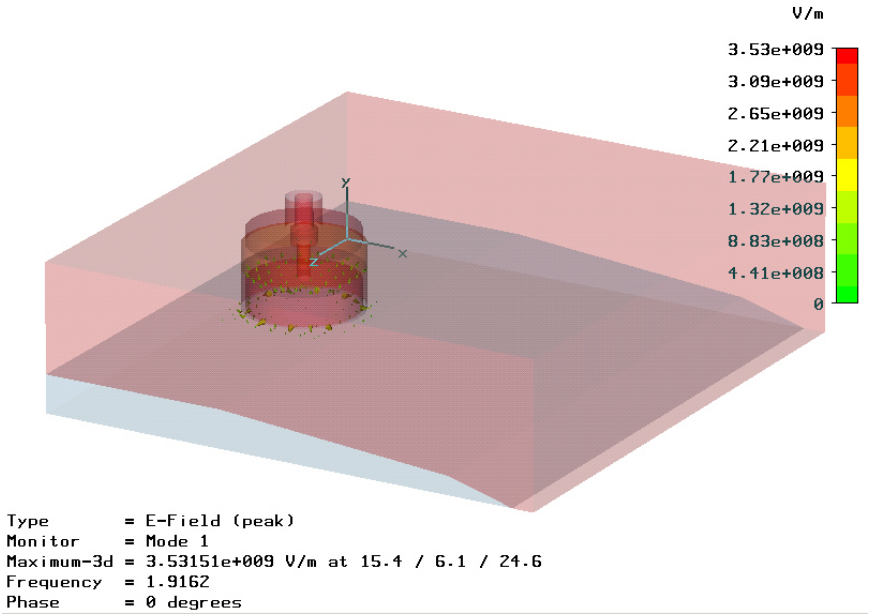

Figure 30: Electric field distribution of the first mode computed with $MWST$.

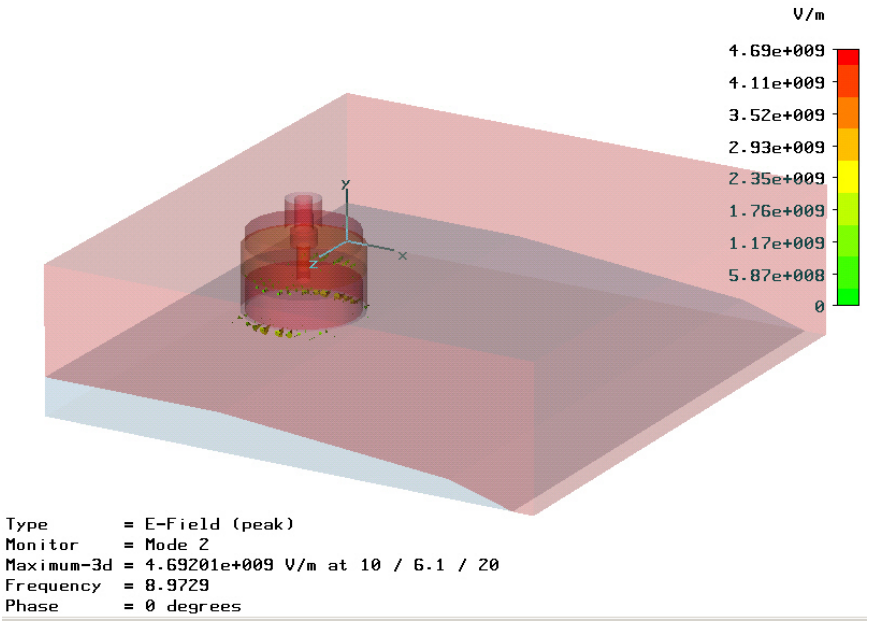

Figure 31: Electric field distribution of the second mode computed with $MWST$.

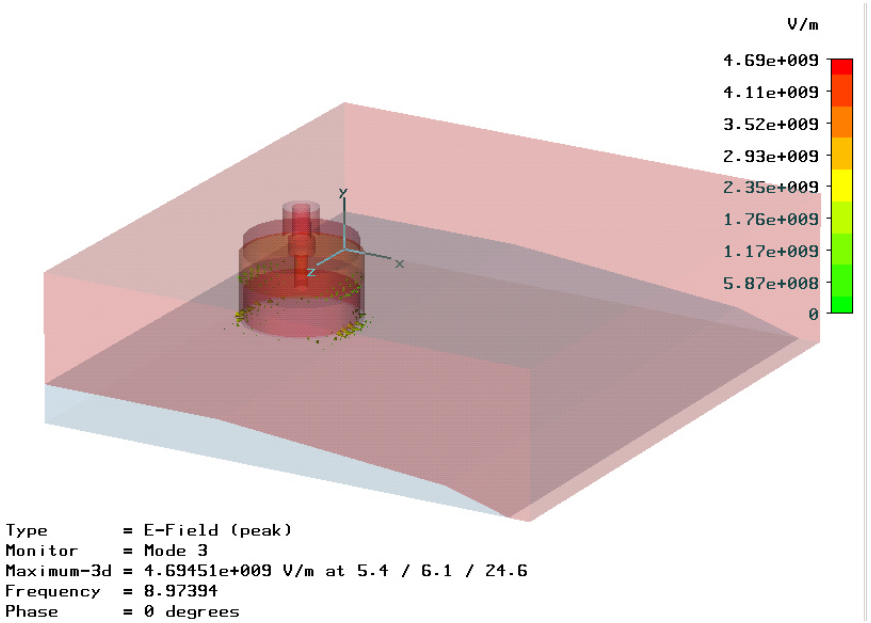

Figure 32: Electric field distribution of the third mode computed with $MWST$..

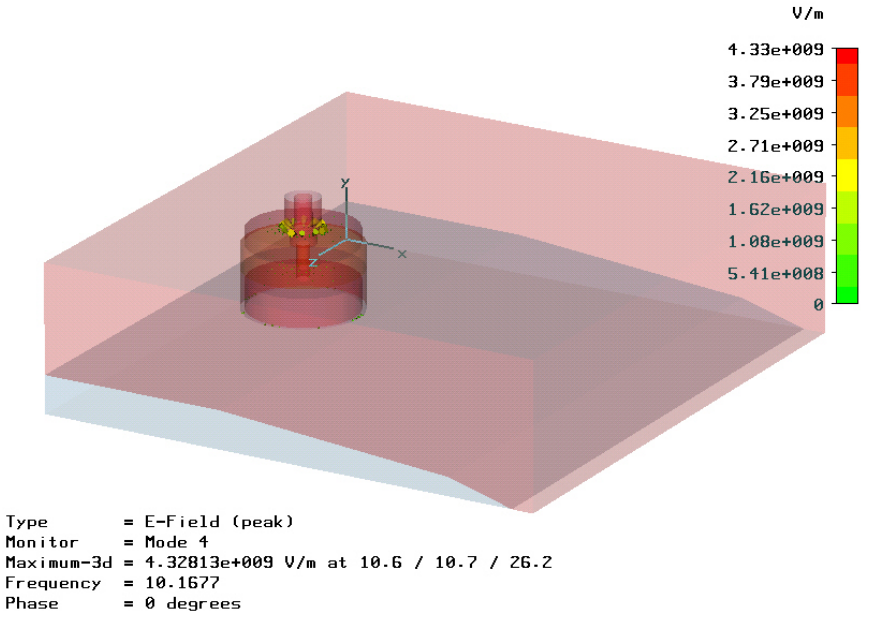

Figure 33: Electric field distribution of the fourth mode computed with $MWST$.

5.1 Wake computations for the BPM in the narrow beam pipe

5.1.1 On axis beam

Half of the beam pipe with two waveguide ports (one at the upper coaxial port and another at the lower coaxial port) has been modeled in $MAFIA$ for the wake computations. The cross section of the narrow beam pipe along with the BPM is shown in Fig. 34. The beam pipe was considered to be 100 mm long. A Gaussian charge distribution with $\sigma = 10$ mm having a total charge of 1 C was taken as the exciting beam. The constant mesh step along z-direction and the fine mesh step around the BPM button were taken as 0.12 mm. The details of the mesh around the BPM button used for the wake computation can be seen in Fig. 35.

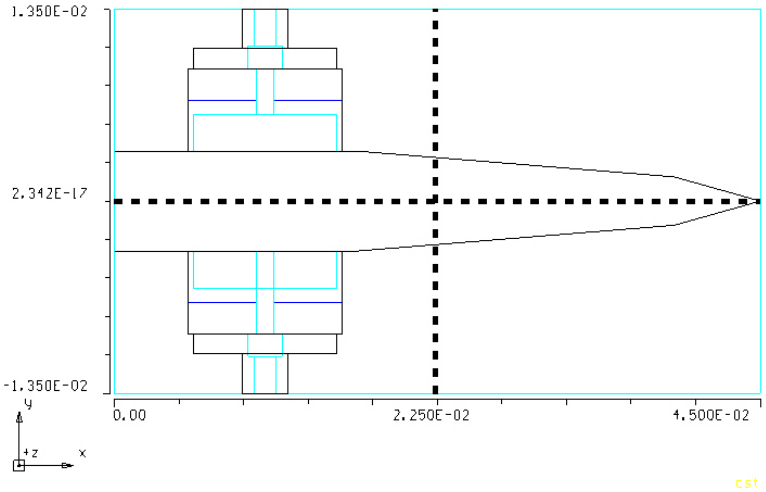

Figure 34: Cross section of the beam pipe and the BPM as modeled with $MAFIA$.

All the components of the wake have been recorded at the position of the beam. Fig. 36 shows the variation of the z-component of the wake with the bunch coordinate for an on axis beam. The output wave amplitudes at both coaxial ports were also recorded, which can be seen in Fig. 37. Although from Fig. 37 at first sight it seems that the output wave amplitudes are the same at the upper and lower coaxial ports, a detailed inspection shows that there is a small difference between the two recorded amplitudes. The details of the output amplitudes and their difference are shown in Fig. 38. It can be noted that the order of magnitude of the difference is much smaller than the peak recorded voltage. This difference is probably caused by a default shift of the y-position of the beam by the $MAFIA$ program. This is again supported by the fact that also a non-zero y-component of the wake field has been found for the on-axis beam as can be seen in Fig. 39.

The total loss parameter (k_{tot}) and $k(1)$-parameter computed according to equations 8 and 9 come out to be -1.6211×10^8 V / C and $-5.2732 \times 10^{10}\ VC^{-1}m^{-1}$, respectively.

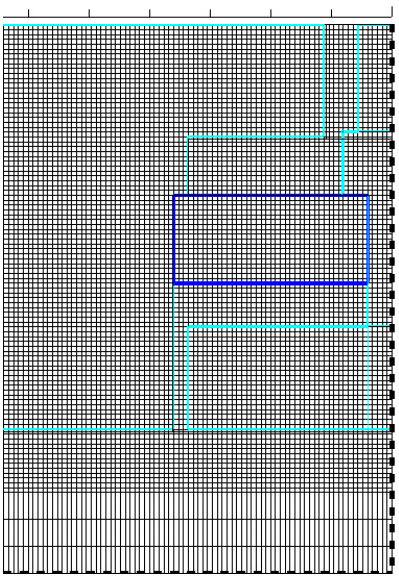

Figure 35: Meshing near the BPM button used in wake computations.

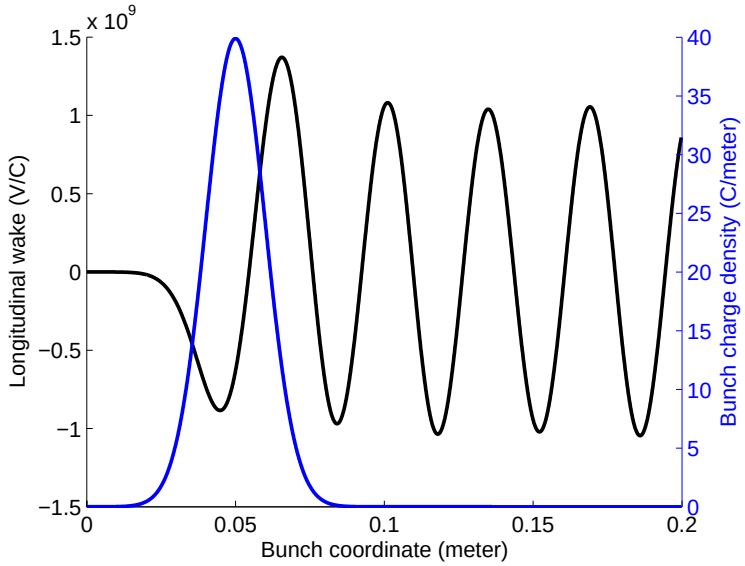

Figure 36: The z-component of the wake and the bunch charge density vs the bunch coordinate (on-axis beam).

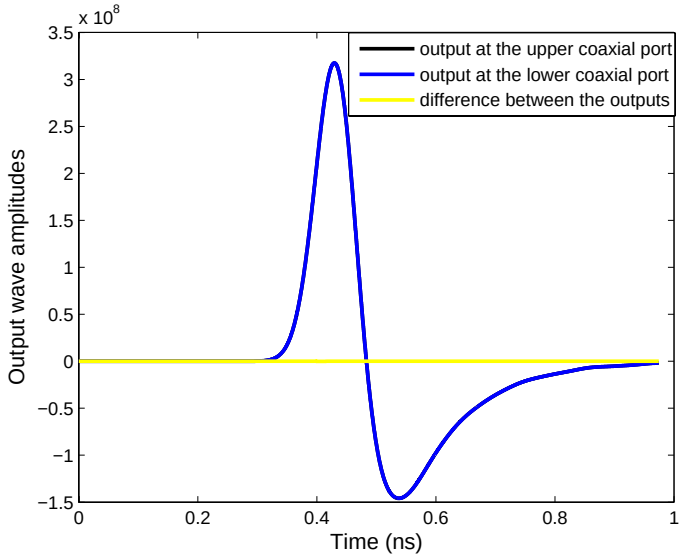

Figure 37: The output wave amplitudes vs time at the coaxial ports for the on-axis beam.

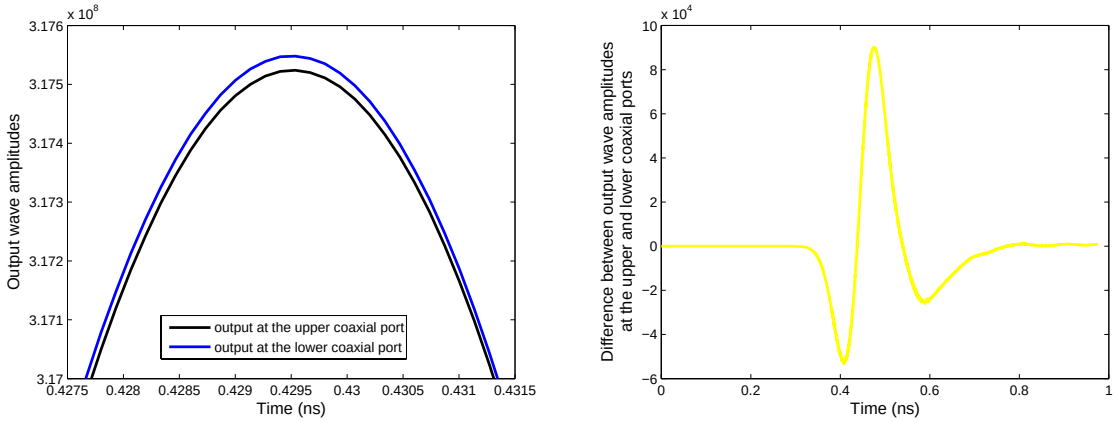

(a) Details of the output wave amplitude at the upper and lower coaxial ports for on axis beam.

(b) Difference between the output wave amplitudes at the upper and lower coaxial ports vs time.

Figure 38: Details of the output wave amplitude at the upper and lower coaxial ports and their difference vs time.

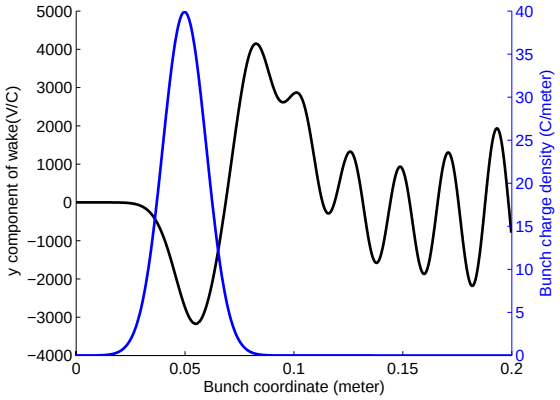

Figure 39: y-component of the wake for the on-axis beam.

5.1.2 Beam with y-offset

In the next step the wakes were estimated for a beam with a y-offset. As the beam pipe in this case is very narrow, a beam offset of 2.0 mm has been used for the y-offset. The geometry of the beam pipe remains the same as shown in Fig. 34. All the components of the wake and the output wave amplitude at the upper and lower coaxial port were recorded. Fig. 40 shows the y and z components of the wake along the beam pipe.

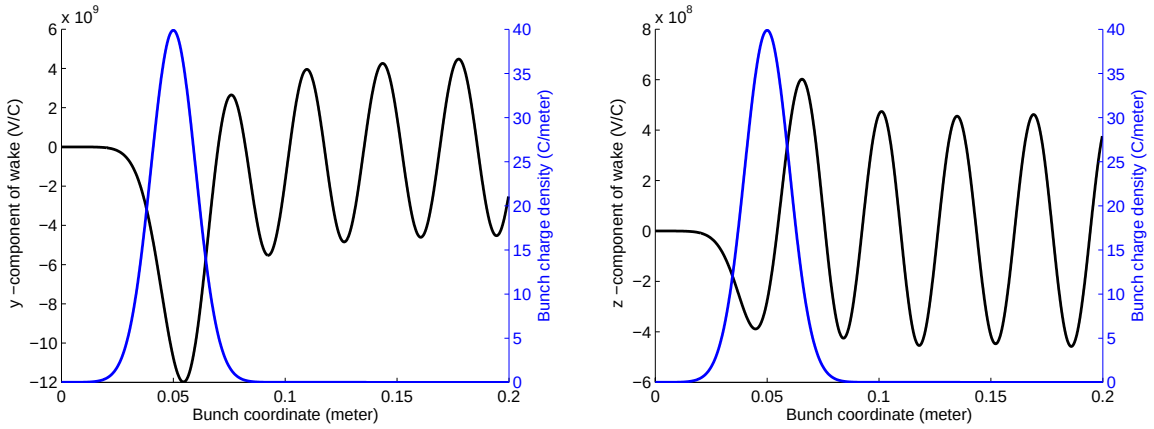

(a) y-component of the wake for the beam with 2 mm y-offset.

(b) z-component of the wake for the beam with 2 mm y-offset.

Figure 40: y- and z- components of the wake along the bunch coordinate for a beam with a y-offset of 2 mm.

Then the total loss parameter was calculated using equation (8). The estimated total loss parameter and $k_{\|}(1)$-parameter come out to be -7.0962×10^{7} V / C and -2.3176×10^{10} $\mathrm{VC^{-1}m^{-1}}$, respectively. The y-kick parameter was computed using equation (10). The y-kick parameter

normalized to an offset of 2 mm in this case is -3.874×10^{12} V/(C m).

6 Summary

Wake computations for the BPMs installed at two different parts of beam tube of PETRA III have been done. The cases of on- and off- axis beams have been considered. $MWST$ and $MAFIA$ were used for the electromagnetic field computations. Wherever possible, agreement between the results from this two codes has been used to validate the results. The issue of trapped modes near in the vicinity of the BPM has also been investigated. Various parameters including different loss parameters and kick parameters have been estimated. The following table summarizes different estimated parameters - which can be used to estimate different beam instabilities as well as the budget for PETRA III.

Analyzed structure	Longitudinal loss parameter (V C^{-1})	y-kick parameter ($VC^{-1}m^{-1}$)	longitudinal $k(1)$ parameter ($VC^{-1}m^{-1}$)
Arc BPM			
Quarter of the arc beam pipe	-4.0744×10^{8}	n.a	-1.0266×10^{11}
Half of the normal beam pipe (offset 5.0 mm)	-3.9167×10^{8}	-1.7842×10^{10}	-9.8876×10^{10}
Quarter of the arc beam pipe (finer mesh)	-3.5276×10^{8}	n.a	-9.0985×10^{10}
Half of the normal beam pipe (offset 5.0 mm) (finer mesh)	-3.3527×10^{8}	-2.5256×10^{10}	-8.6656×10^{10}
Undulator BPM			
Half of the narrow beam pipe (offset 0 mm)	-1.6211×10^{8}	-1.9147×10^{3}	-5.2732×10^{10}
Half of the narrow beam pipe (offset 2 mm)	-7.0962×10^{7}	-3.8739×10^{12}	-2.3176×10^{10}

Table 13: Summary of the various loss parameters and kick parameters.

The results for the arc BPM was first obtained using a mesh with a step size of 0.12 mm along the z-axis and a step size of 0.8 mm for the transverse dimensions. In the region of the BPM buttons a step size of 0.12 mm was also used for the transverse dimensions. The wake calculations have been repeated on a finer mesh with a step size of 0.1 mm along the z-axis

and a step size of 0.5 mm for the transverse dimensions. In this case a step size of 0.1 mm was used in the region of the BPM buttons. The results for the BPM in the undulator pipe in Table 13 were obtained with the fine mesh.

Acknowledgment

We would like to thank Mark Lomperski for carefully reading the manuscript.

References

[1] K. Balewski, W. Brefeld, W. Decking, H. Franz, R. Röhlsberger, E. Weckert, Eds. PETRA III: A low emittance synchrotron radiation source. Technical Design Report, DESY 2004-035, February 2004.

[2] M. Phillips W.K.H. Panofsky. *Classical Electricity and Magnetism*. Addison-Wesley, Reading, MA., 1962.

[3] P. B. WILSON. Introduction to wakefields and wake potentials. U.S. Particle Accelerator School, Batavia, Illinois, July-August 1987.

[4] B.W. Zotter and S. Kheifets. *Impedances and Wakes in High Energy Particle Accelerators*. World Scientific, London, 1998.

[5] T. Weiland and R. Wanzenberg. Wakefields and impedances. Joint US-CERN particle accelerator school, Hilton Head Island, SC, USA, November 1990. Edited by M. Dienes, M. Month and S. Turner.

[6] T. Weiland. Parasitic energy loss due to cavities in PETRA. Internal Report M-81/04, DESY, 1981.

[7] T. Weiland. PETRA's impedance. Internal Report M-81/23,DESY,1981.

[8] K. Balewski. Analyse der transversalen Moden-Kopplungsinstabilität für lokalisierte HF-Strukturen und ihre Kompensierbarkeit durch Rückkopplungssysteme. DESY 89-108, Aug. 1989.

[9] CST microwave studio. Version 5, March 2005. CST GmbH.

[10] T. Weiland. A discretization method for the solution of maxwell's equations for six-component fields. *Electronics and Communication,(AEÜ)*, 31:116, 1977.

[11] T. Weiland. Numerical solution of maxwell's equations for static, resonant and transient problems. In *International URSI Symposium on Electromagnetic Theory*, pages 537–542, Budapest, August 1986.

[12] MAFIA. Release 4, Nov 2004. CST GmbH.